



Cite this: *Energy Environ. Sci.*, 2016, 9, 3754

# Electronic and nuclear contributions to time-resolved optical and X-ray absorption spectra of hematite and insights into photoelectrochemical performance†

Dugan Hayes,<sup>\*a</sup> Ryan G. Hadt,<sup>a</sup> Jonathan D. Emery,<sup>b</sup> Amy A. Cordones,<sup>c</sup> Alex B. F. Martinson,<sup>b</sup> Megan L. Shelby,<sup>ad</sup> Kelly A. Fransted,<sup>a</sup> Peter D. Dahlberg,<sup>ae</sup> Jiyun Hong,<sup>ad</sup> Xiaoyi Zhang,<sup>f</sup> Qingyu Kong,<sup>f</sup> Robert W. Schoenlein<sup>c</sup> and Lin X. Chen<sup>\*ad</sup>

Ultrafast time-resolved studies of photocatalytic thin films can provide a wealth of information crucial for understanding and thereby improving the performance of these materials by directly probing electronic structure, reaction intermediates, and charge carrier dynamics. The interpretation of transient spectra, however, can be complicated by thermally induced structural distortions, which appear within the first few picoseconds following excitation due to carrier–phonon scattering. Here we present a comparison of *ex situ* steady-state thermal difference spectra and transient absorption spectra spanning from NIR to hard X-ray energies of hematite thin films grown by atomic layer deposition. We find that beyond the first 100 picoseconds, the transient spectra measured for all excitation wavelengths and probe energies are almost entirely due to thermal effects as the lattice expands in response to the ultrafast temperature jump and then cools to room temperature on the microsecond timescale. At earlier times, a broad excited state absorption band that is assigned to free carriers appears at 675 nm, and the lifetime and shape of this feature also appear to be mostly independent of excitation wavelength. The combined spectroscopic data, which are modeled with density functional theory and full multiple scattering calculations, support an assignment of the optical absorption spectrum of hematite that involves two LMCT bands that nearly span the visible spectrum. Our results also suggest a framework for shifting the ligand-to-metal charge transfer absorption bands of ferric oxide films from the near-UV further into the visible part of the solar spectrum to improve solar conversion efficiency.

Received 4th August 2016,  
Accepted 28th October 2016

DOI: 10.1039/c6ee02266a

[www.rsc.org/ees](http://www.rsc.org/ees)

### Broader context

Photocatalytic materials for industrial-scale generation of solar fuels must exhibit excellent long-term stability and be comprised of earth-abundant materials. Hematite, a photoelectrocatalyst for water oxidation, meets these criteria but performs poorly in the visible part of the solar spectrum. Despite the simple nature of this material, the assignment of the steady-state absorption bands remains actively debated in the literature, and no experimental work has directly identified which optical transitions are photochemically active. Herein, we report a series of ultrafast transient absorption and steady-state variable temperature spectroscopic measurements of hematite that allow us to resolve these two issues. We identify two distinct ligand-to-metal charge transfer bands and demonstrate that these transitions contribute equally to the photocatalytic performance of hematite while the weaker d–d transitions do not. Furthermore, we find that *ex situ* ultrafast transient absorption spectra of hematite are dominated by thermal effects arising from laser-induced heating and show that these contributions must be carefully taken into account when performing ultrafast measurements of samples in the solid state.

<sup>a</sup> Chemical Sciences and Engineering Division, Argonne National Laboratory, Argonne, IL 60439, USA. E-mail: [hayesd@anl.gov](mailto:hayesd@anl.gov), [lchen@anl.gov](mailto:lchen@anl.gov)

<sup>b</sup> Materials Science Division, Argonne National Laboratory, Argonne, IL 60439, USA

<sup>c</sup> Chemical Sciences Division, Lawrence Berkeley National Laboratory, Berkeley, CA 94709, USA

<sup>d</sup> Department of Chemistry, Northwestern University, Evanston, IL 60208, USA

<sup>e</sup> Graduate Program in the Biophysical Sciences, The James Franck Institute, and The Institute for Biophysical Dynamics, The University of Chicago, Chicago, IL 60637, USA

<sup>f</sup> X-ray Science Division, Argonne National Laboratory, Argonne, IL 60439, USA

† Electronic supplementary information (ESI) available: Sample preparation, experimental and computational details, tabulated fitting parameters, optical reflectance correction, comparisons of transient spectra at different excitation wavelengths, and additional supporting figures. See DOI: 10.1039/c6ee02266a

## Introduction

Earth abundant heterogeneous photocatalysts for oxygen and hydrogen evolution provide a practical means of generating carbon-free solar fuels, and a detailed understanding of the photophysical properties of these materials is crucial for the rational design of higher performing devices.<sup>1</sup> To this end, time-resolved investigations of photocatalytic metal oxide semiconductors spanning from the femtosecond to the millisecond regime have provided insight into the mechanisms of charge separation, diffusion, and interfacial transfer in these systems.<sup>2–7</sup> In optical transient absorption (OTA) experiments, transition states and reaction intermediates may be directly monitored from excited state absorption (ESA) and stimulated emission (SE) signals, while charge recombination rates may be deduced from the recovery of ground state bleach (GSB) features.<sup>8</sup> In often complementary fashion, X-ray transient absorption (XTA) experiments at the metal K-edge can reveal transient changes in the oxidation state and local environment of the metal center as charge separation and polaron formation occur,<sup>9</sup> while ligand (*e.g.* O, N, or S) K-edge XTA experiments can reveal changes in covalency by probing pre-edge transitions to bound states of mixed metal–ligand character.<sup>10,11</sup> Understanding and quantifying ultrafast charge recombination processes is of utmost importance for improving the efficiency of photocatalytic and photoelectrocatalytic materials, but despite the great promise of these techniques in this capacity, it is often challenging in practice to extract the transient signals of interest from those of thermal origin. Even at very low fluences, a laser pulse indirectly deposits an enormous amount of thermal energy into a semiconductor upon band gap excitation by generating hot carriers that cool through carrier–phonon scattering.<sup>12</sup> The additional thermal disorder and attendant lattice expansion<sup>13,14</sup> can narrow the band gap of the material, resulting in the appearance of a strong positive feature in the OTA spectrum at energies at or below the band gap.<sup>15–17</sup> These effects also introduce additional broadening and multiple scattering phase shifts in X-ray absorption near edge structure (XANES) measurements,<sup>18–21</sup> again resulting in the appearance of thermal transient signals.

In this work, we model and follow the evolution of the thermal contributions to the transient absorption signals of hematite thin films grown by atomic layer deposition (ALD)<sup>22</sup> in the near-IR (NIR), optical, soft X-ray, and hard X-ray regimes. Hematite ( $\alpha\text{-Fe}_2\text{O}_3$ ) is a remarkably stable and inexpensive water oxidation photoelectrocatalyst with absorption extending into the NIR and a valence band potential capable of driving the oxygen evolution reaction at high pH.<sup>23,24</sup> The utility of hematite is limited, however, by weak absorption at wavelengths longer than 550 nm coupled with poor carrier mobility and rapid photocarrier recombination.<sup>25–28</sup> As a result of these deficiencies, hematite does not exhibit photochemical water oxidation in the absence of a large oxidative overpotential. Nanostructuring has proven a successful approach to increasing the effective optical density of hematite-based photoanodes while maintaining minimal material thicknesses to minimize recombination losses.<sup>29–33</sup>

Nevertheless, even thin films grown by ALD and electrodeposition exhibit incident and absorbed photon-to-current efficiency (IPCE and APCE, respectively) spectra that drop steeply going from 375 to 550 nm and reach zero for wavelengths longer than 600 nm.<sup>5,31,34</sup> Efforts to overcome these deficiencies would greatly benefit from a detailed understanding of the electronic transitions in hematite, but the assignment of the optical bands of this material remains actively debated. While the weak absorption features in the red and NIR have generally been assigned to spin-forbidden d–d (ligand field) transitions and the strong absorption features in the blue and near-UV (NUV) to ligand-to-metal charge transfer (LMCT) transitions,<sup>35–38</sup> recent publications have positioned the LMCT bands everywhere from 200 nm<sup>39</sup> to 700 nm.<sup>40–42</sup> Chernyshova *et al.* have collected many of the frequencies and assignments of the optical absorption bands of hematite reported in the literature over several decades, demonstrating the great diversity of models proposed for the electronic structure of this material.<sup>43</sup> And while a combination of *ex situ* and *in situ* steady-state and time-resolved measurements have provided evidence to support the assignment of transitions at particular wavelengths, the features in the spectra obtained by these methods present another set of difficult assignments.

Hematite thin films and nanoparticles have been extensively studied *ex situ* by ultrafast OTA with the goal of addressing these issues. Zhang and coworkers reported transient measurements of hematite nanoparticles following excitation at 390 nm and found that the decay of the spectra could be fit with a triexponential model with time constants of 0.36, 4.2, and 67 ps, finding no transient signal beyond 100 ps.<sup>2</sup> Furthermore, they found these lifetimes to be independent of both pump fluence and probe wavelength, concluding that a high density of trap states results in rapid (sub-ps) carrier trapping followed by non-radiative recombination. Using 100 nm thin films grown by molecular beam epitaxy, Joly *et al.* also observed a sub-ps and a few-ps component in transient signals, which were assigned to carrier thermalization to the conduction band edge and subsequent trapping and recombination.<sup>3</sup> However, they also observed a strong signal that persisted well beyond the  $\sim 100$  ps window of the experiment, which was assigned to long-lived trap states, including mid-gap d–d states. Huang *et al.* extended the temporal window of these experiments by measuring the transient spectra of hematite thin films grown by ALD at delay times spanning from the sub-ps to the  $\mu\text{s}$  regime.<sup>5</sup> In addition to measuring lifetimes consistent with the earlier work, they reported several additional time constants in the ns and  $\mu\text{s}$  regimes that they assign to long-lived photocarriers responsible for the oxygen evolution reaction.

Both Huang *et al.* and Durrant and coworkers<sup>6,44,45</sup> have reported spectroelectrochemical measurements to support assignment of the OTA features, showing a strong feature at 580 nm under anodic bias that overlaps well with the primary positive peak observed in the OTA spectra. This feature was assigned by Durrant and coworkers to absorption from the valence band to mid-gap states, while an additional transient feature observed at long times ( $> 1$  ms) only under anodic bias was assigned to

absorption within the valence band to photoholes generated by the initial excitation ("hole filling"). The authors also note that some of the latter ESA may also correspond to absorption by conduction band electrons, as assigned by Huang *et al.*<sup>5</sup> and Dawlaty and coworkers.<sup>46</sup> The magnitudes and lifetimes of both features were found to be strongly dependent on the external potential, suggesting that the applied field is necessary to segregate photocarriers to prevent recombination and facilitate the oxygen evolution reaction, which requires a coulombically daunting four redox equivalents. More recently, Durrant and coworkers have reported *in situ* spectroelectrochemical transient absorption measurements conducted on the ultrafast time-scale and similarly observed a retardation of transient decay under anodic bias.<sup>47</sup>

In the hard X-ray regime, Katz *et al.* have reported XTA measurements of dye-sensitized hematite nanoparticles and found transient signals consistent with the formation of electron small polarons in the hematite lattice following excitation of the surface bound dye and subsequent injection of photoelectrons into the nanoparticle.<sup>48–50</sup> And most recently, Vura-Weis *et al.* have reported transient iron  $M_{2,3}$ -edge measurements of hematite thin films with sub-ps resolution, capturing the appearance and decay of a transient  $Fe^{2+}$  species with a lifetime of 240 fs following excitation at 400 nm.<sup>51</sup> This experiment demonstrates that oscillator strength at 400 nm is dominated by LMCT intensity but also highlights one of the biggest challenges in investigating this system using time-resolved spectroscopy: the excited state species most informative with respect to interpreting the absorption spectrum are only clearly observable for less than 1 ps.

In this report we demonstrate through a battery of transient absorption studies conducted at a range of excitation wavelengths and fluences and corresponding variable temperature measurements that transient signals at time delays beyond the first picosecond are dominated by thermal contributions, including lattice expansion and thermal disorder, arising from carrier-phonon scattering following excitation of hot carriers. Lifetimes longer than 100 ps previously reported in *ex situ* transient absorption measurements were assigned to slow recombination of charge carriers, but we instead find that carrier recombination in the absence of an applied bias is complete within 100 ps and these lifetimes may instead be attributed to lattice distortion and cooling processes. The presence of strong thermally-derived signals complicates the assignment of decay components and excited state absorption features and obfuscates transient signals corresponding to photocarriers. Nevertheless, we provide a fit to both the thermal and photoinduced optical difference spectra that provides support for an assignment of the LMCT and d-d bands in the optical absorption spectrum. The assignments of the steady-state and time-resolved features are supported by oxygen K-edge XTA measurements as well as density functional theory calculations. XTA and variable temperature measurements at the iron K-edge also reveal contributions from both lattice expansion and thermal disorder. A comparison of the kinetics obtained from OTA measurements spanning from 200 fs to 30 ms to those obtained for a solution-phase iron(III) complex

reveal a short-lived (< 100 ps) ESA signal that is distinct from the thermal difference spectrum at early times that may be uniquely assigned to photocarriers, while the timescale of lattice expansion is found to be  $\sim 1$  ns. The cooling of the lattice back to room temperature occurs with complex kinetics spanning six orders of magnitude in time with a small transient remaining even at 25  $\mu$ s. The band gap shrinkage that results from lattice expansion is found to push the calculated IPCE spectrum toward lower energies in the visible part of the spectrum, suggesting a possible scheme for improving the efficiency of oxygen evolution at hematite photoanodes under solar illumination.

## Results

### 1. Steady state and transient optical absorption

The reflectance-corrected steady-state optical absorption spectrum of a 20 nm hematite thin film was fit to the sum of seven Gaussian functions using previously reported transition frequencies of bulk hematite<sup>37</sup> as initial guesses (see Section S3 of the ESI† and Fig. S1 for a discussion of reflectance-correction, ESI†). We note that at least seven bands were required to obtain a uniformly good fit across the entire absorption spectrum. The results of the fit are shown in Fig. 1 and collected in Table S1 (ESI†), showing excellent agreement with those measured and collected from the literature by Chernyshova *et al.*<sup>43</sup> Five minor bands, shown in color, are distributed across the visible region. These bands are assigned to single and pair ligand field (d-d) spin-flip transitions, which gain some oscillator strength from the superexchange interaction between neighboring  $Fe^{3+}$  sites.<sup>38,52</sup> We note that the band at 4.30 eV is significantly broader than the others and may likely correspond to two or more transitions

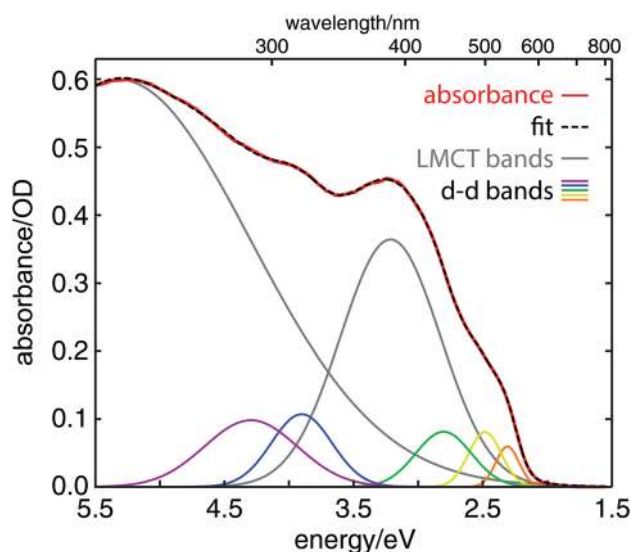


Fig. 1 The reflectance-corrected steady-state optical absorption spectrum of a 20 nm hematite thin film (red). The spectrum was fit (dashed black) to the sum of seven Gaussian bands, which are plotted individually. The absorption bands assigned to LMCT transitions are shown in gray, and those assigned to d-d transitions are shown in color. The fit parameters are collected in Table S1 (ESI†).

that have been assigned in this region.<sup>38</sup> The fit is dominated, however, by the two strong bands shown in gray at 3.22 eV (385 nm) and 5.32 eV (233 nm), which are identified as LMCT transitions in accordance with previous experimental and theoretical reports.<sup>35–37,43</sup> Following the complete active space calculations on hematite clusters reported by Liao and Carter, these bands are assigned to the weaker out-of-plane ( $O\ 2p \rightarrow t_{2g}$ , OOP) and stronger in-plane ( $O\ 2p \rightarrow e_g$ , IP) transitions, respectively.<sup>39</sup> In the context of this assignment, the relative linewidths and oscillator strengths of these bands are also consistent with the oxygen K-edge XAS spectrum and the DFT calculations presented in this report (*vide infra*).

The OTA spectrum measured at a delay time of 20 ps with a pump wavelength of 415 nm (2.99 eV) at a fluence of  $30\ \text{mJ cm}^{-2}$  is shown (dashed blue) in Fig. 2 (see Section S4 of the ESI† for experimental details and Section S3 and Fig. S3 for a discussion of the effects of transient reflectance in the OTA experiments, ESI†). A thermal difference spectrum (the difference of the steady-state spectra measured at 500 K and 300 K) is also presented (solid red), with the OTA spectrum scaled by a factor of 0.25 to facilitate comparison. Both spectra share a highly structured negative region at shorter wavelengths (labeled B and C) and a strong positive band with a maximum at  $\sim 575\ \text{nm}$  (D), the same features previously reported in OTA data.<sup>5,50</sup> While the relative magnitudes of the features differ slightly between the photoinduced and thermal difference spectra, the qualitative agreement in the visible region (300–800 nm) is striking, suggesting that the OTA spectrum is dominated by thermal effects as early as 20 ps. Pumping the sample at 415 nm (3.0 eV) is expected to excite primarily the OOP LMCT transition, yielding transient electron small polarons<sup>49</sup> while concurrently heating the lattice through carrier-phonon scattering.<sup>12</sup>

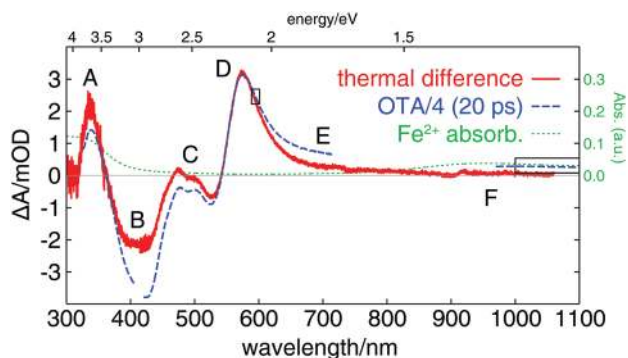


Fig. 2 The thermal difference spectrum, obtained by taking the difference of the steady-state spectra measured at 500 K and 300 K (solid red), plotted alongside the OTA spectrum measured at a delay time of 20 ps with a pump wavelength of 415 nm (dashed blue). The OTA spectrum is scaled by a factor of 0.25 to facilitate comparison. The region between 730 and 930 nm is inaccessible in the OTA experiment due to proximity to the Ti:Sapph fundamental at 830 nm used to generate the visible and NIR continuum probes. The absorption spectrum of  $[\text{Fe}(\text{H}_2\text{O})_6]^{2+}$  is also given (dotted green) to show the position and shape of the NIR spin-allowed d–d transitions expected for transient  $\text{Fe}^{2+}$  species. The regions binned to give the kinetic traces in Fig. 8 are enclosed by black boxes. Features referenced in the main text are labeled A–F.

Both the  $\text{Fe}^{2+}$  centers and the distorted  $\text{Fe}^{3+}$  sites in the second shell surrounding them would exhibit absorption spectra different from that of the ground state, and these transient species likely contribute some amplitude to the observed OTA spectrum. This could account for the disparity between the difference spectra near 400 nm (B), but the number and complexity of transitions expected for these high spin, anti-ferromagnetic species in that region impedes making conclusive assignments.<sup>53</sup> At least some of this difference may be attributed to transient GSB and/or SE signals, which contribute additional negative amplitude near region C as discussed in Section 5 below. Meanwhile, the broad positive band (D) in the thermal spectrum extends only very weakly beyond 700 nm, reaching the baseline by 900 nm, while the positive signal in the optical experiment spans the NIR (F) out to the limits of our detection at 1600 nm, as shown in Fig. S2 (ESI†). The positive laser-induced signal in the NIR overlays well with the broad spin-allowed d–d band measured in aqueous  $[\text{Fe}(\text{H}_2\text{O})_6]^{2+}$  (dotted green),<sup>54</sup> suggesting that some part of this feature may correspond to similar d–d transitions in the intermediate spin  $\text{Fe}^{3+}$  and high spin  $\text{Fe}^{2+}$  transient species that appear following d–d and LMCT transitions (a more thorough assignment of free carrier absorption in this region is given in the Discussion).

To determine if an individual laser pulse deposits sufficient energy into the hematite sample to raise the temperature enough to account for the strong OTA signal, we carefully measured the laser fluence at the sample under conditions that exactly reproduce the magnitude of the thermal difference spectrum at 575 nm (see Section S5 of the ESI† for a detailed discussion of this measurement and calculation). We find that the maximum temperature increase from this pump fluence is  $\sim 470\ \text{K}$ . Some of the laser energy will be dissipated by non-thermal (e.g. photochemical) pathways, and some thermal energy is also expected to be transferred into the quartz substrate. These factors likely account for the difference between the calculated maximum temperature increase and the 200 K temperature increase used in the steady state measurement to obtain the same signal magnitude. Overall, we find that the laser deposits more than enough energy into the sample than is required to account for the temperature increase used to obtain the steady state difference spectrum, and we conclude that our thermal model is fully consistent with a simple equilibrium consideration of the temperature of the film upon laser excitation.

To uncover the origin of the photoinduced and thermal absorption features in the visible region, we endeavored to fit the difference spectra to the function given by eqn (1), *i.e.* the difference between the fit to the steady-state absorption spectrum (Fig. 1) and a modified steady-state fit (denoted with a prime) in which the frequencies ( $\nu_i$ ), linewidths ( $c_i$ ), and amplitudes ( $B_i$ ) of the absorption bands were allowed to vary:

$$\Delta A(\nu) = \sum_i \left( B'_i \exp\left(\frac{-(\nu - \nu'_i)^2}{2c_i'^2}\right) - B_i \exp\left(\frac{-(\nu - \nu_i)^2}{2c_i^2}\right) \right) \quad (1)$$



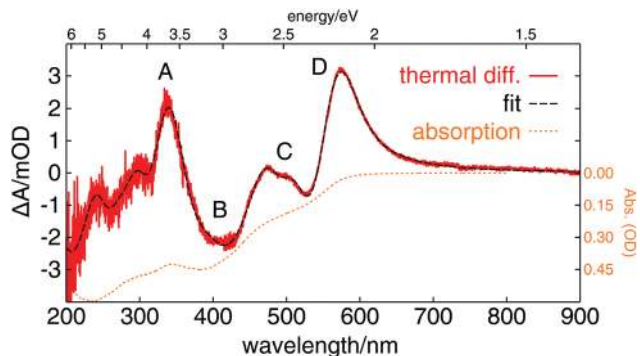


Fig. 3 The thermal difference spectrum of hematite (red) and the fit (dashed black) obtained using eqn (1) and the steady-state fit shown in Fig. 1. The inverted steady-state absorption spectrum is given as a reference (dotted orange). The fit parameters are collected in Table S2 (ESI<sup>†</sup>). Features referenced in the main text are labeled A–D.

Because the detected white light continuum probe does not extend beyond 315 nm (3.9 eV) and the strongest absorption band is centered at 233 nm (5.3 eV), attempts to fit the OTA spectrum were very sensitive to initial guesses and generally gave spectra with unreasonably large ( $>100$  mOD) features in the UV. The thermal difference spectrum, however, could be measured out to 200 nm (6.2 eV), and consequently the fit readily converged to a single solution for this simple model for a broad range of initial guesses. The fit is shown in Fig. 3 with the inverted steady-state spectrum provided as a reference, and the results are collected in Table S2 (ESI<sup>†</sup>). Because the two difference spectra qualitatively exhibit the same features and the OTA spectrum is underdetermined, we provide here an analysis of the fit to the thermal difference spectrum with the assumption that largely the same picture may be used to describe the transient features in the visible regime at delay times beyond a few ps, *i.e.* following thermalization.

The individual absorption bands from the steady-state fit (solid lines) and the thermal difference spectrum (dashed lines) are shown in Fig. 4. The gray LMCT bands both exhibit a modest broadening and bathochromic shift, with the lower energy OOP transition broadening and shifting more than the IP transition. These shifts result in a net increase in the ligand field splitting  $10 Dq$  of  $180 \text{ cm}^{-1}$  (0.02 eV), which is then expected to impact the positions of some of the d–d transitions. Predicting these resultant d–d shifts from the  $d^5$  Tanabe–Sugano diagram, however, is complicated by the superexchange-mediated nature of the spin–flip transitions. Thermal occupation of higher-lying states in the  $\text{Fe}^{3+}$  pair spin manifold may shift the center of the transition depending on the relative magnitudes of the exchange integrals of the ground and excited state ion pairs, while the exchange integrals themselves may also shift as a result of thermally induced structural distortion and thus change the peak positions and amplitudes. Nevertheless, it is clear, perhaps unsurprisingly, that the fine structure observed between 460 and 550 nm (C) originates from thermally induced changes in the three d–d bands that lie in this region.

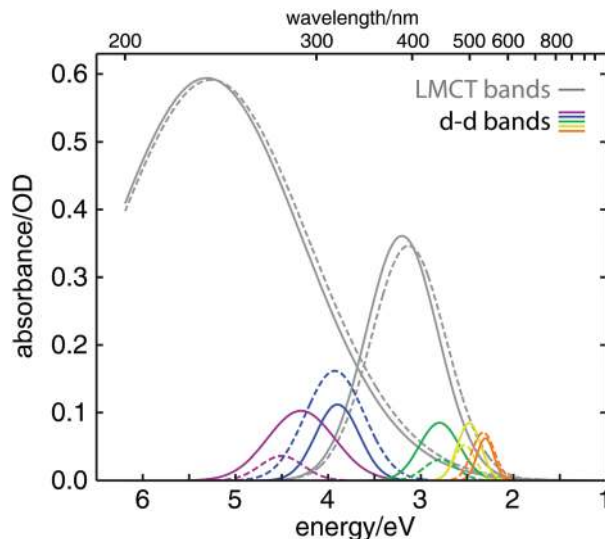


Fig. 4 The individual components of the fits of the steady-state absorption spectrum shown in Fig. 1 (solid lines) and the thermal difference spectrum (dashed lines) shown in Fig. 3.

More notably, the fit demonstrates that peak D at 575 nm in the thermal difference spectrum (Fig. 3), and thus presumably the nearly identical positive feature observed in the OTA spectrum, originates partially from these d–d bands as well. The LMCT (solid blue) and d–d (dashed red) contributions to the fit are plotted separately in Fig. 5, demonstrating that the structure observed in the difference spectrum generally arises from the interference between the bleaching of the d–d bands and the redistribution of LMCT intensity to lower energies. In particular, the sharp asymmetry of the 575 nm band (D) seen in Fig. 2 and 3 arises from an increase in intensity of the lowest energy d–d band overlapping with the tail of the shifted LMCT intensity that extends beyond the bleaching of the other d–d bands. These contributions are highlighted with a green box in Fig. 5. This feature was also investigated in the OTA spectrum by monitoring

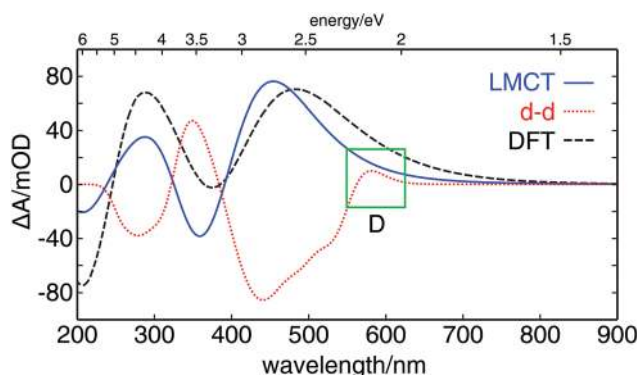


Fig. 5 The thermal difference spectra calculated for only the LMCT transitions (blue) and d–d transitions (dashed red) as obtained from the fit shown in Fig. 3. The difference spectrum obtained from DFT calculations modeling the thermal expansion of hematite in  $[\text{Fe}(\text{H}_2\text{O})_6]^{3+}$  (black) shows good qualitative agreement with the calculated LMCT difference spectrum. The green box highlights the origin of peak D from Fig. 2 and 3.

the position of the peak as a function of pump fluence, as shown in Fig. S4 (ESI<sup>†</sup>), in which the spectra are normalized to their respective maxima. As pulse energy (and thus the lattice temperature) is increased from 0.20 to 1.5  $\mu\text{J}$  per pulse ( $0.75\text{--}5.7\text{ mJ cm}^{-2}$  fluence), the magnitude of the signal increases and the 575 nm peak shifts further toward the red end of the spectrum as the OOP LMCT band continues to broaden and shift. We note that aside from this subtle shift, even at an energy of only 200 nJ ( $0.75\text{ mJ cm}^{-2}$ ), the overall shape of the normalized OTA spectrum is the same as at other energies, demonstrating that lattice heating remains the dominant source of transient signal even under very weak illumination.

## 2. Density functional theory calculations

To confirm our assignments, we examined the effect of lattice heating on the electronic structure by performing DFT and time-dependent DFT (TD-DFT) calculations on a single  $[\text{Fe}(\text{H}_2\text{O})_6]^{3+}$  complex with Fe–O bond lengths distorted to match the geometry of hematite. Despite the simplicity of this model, it proves helpful here because it describes the local electronic structure of the  $\text{Fe}^{3+}$  center when superexchange between  $\text{Fe}^{3+}$  ion pairs and spin flip transitions are excluded. It therefore provides us with a difference spectrum that approximates the isolated LMCT difference spectrum as shown in Fig. 5. An individual  $\text{Fe}^{3+}$  center in bulk hematite has  $C_{3v}$  symmetry, with three long (2.11 Å) and three short (1.95 Å) Fe–O bonds in the *fac* orientation.<sup>55</sup> Variable temperature powder diffraction data reported by Gualtieri *et al.* at 300 and 1050 K show that the Fe–O bond distances lengthen asymmetrically upon heating, with the long bonds increasing 2.8 times more than the short bonds.<sup>56</sup> For our DFT calculations, then, we began with the optimized octahedral geometry of  $[\text{Fe}(\text{H}_2\text{O})_6]^{3+}$  and moved three  $\text{H}_2\text{O}$  ligands +0.08 Å and the other three –0.08 Å from the center to match the bulk geometry at room temperature before calculating the absorption spectra. The ligands were similarly moved +0.090 and –0.076 Å to simulate the thermally expanded lattice.

The major transitions obtained from the TD-DFT calculations can be readily grouped into IP and OOP LMCT bands, but there are also a number of weak transitions that appear at energies distributed between the two bands as the octahedral symmetry is broken, which facilitates the distribution of oscillator strength over transitions that are near-by in energy. The oscillator strength calculated for the IP LMCT band is 3.4 times that of the OOP band, in fair agreement with the value of 4.3 obtained from the steady-state absorption spectrum. While the center frequency of the OOP band matched the value from the absorption spectrum, the IP band was significantly (2.17 eV) higher in energy. This disagreement stems from the substitution of waters for the oxo ligands and the treatment of the frontier orbitals of an individual ion instead of the valence and conduction bands of the bulk material. Protonation will of course contribute to the IP/OOP energy splitting between the different donor orbitals but nevertheless still provides a good methodology to monitor the resulting LMCT intensities and splitting as a function of structural perturbations. Accordingly, the IP transitions were shifted down by 2.17 eV, and the

resulting room temperature stick spectrum was Gaussian broadened to reproduce the LMCT bands obtained from the steady-state spectrum (FWHM = 1.0 and 2.0 eV for the OOP and IP bands, respectively). The 1050 K stick spectrum was then broadened by the same amount, and the resulting difference spectrum is scaled and plotted (dashed black) alongside the LMCT difference spectrum in Fig. 5, showing good qualitative agreement. The individual Gaussian broadened spectra are given in Fig. S5 (ESI<sup>†</sup>), showing that the calculation reproduces the thermal bathochromic shifts and broadenings as well as the relative magnitudes of the changes for the two bands.

## 3. Oxygen K-edge transient absorption

Further confirmation of the LMCT assignments of the steady-state, thermal, and OTA absorption spectra may be found through an analysis of the X-ray absorption spectrum at the oxygen K-edge. The oxygen pre-edge in hematite is split into two well-resolved peaks, corresponding to transitions to the oxygen 2p orbitals mixed with the iron 3d orbitals.<sup>57–59</sup> The two peaks, then, correspond to the 1s to 2p transitions mixed with the  $t_{2g}$  and  $e_g$  3d orbitals and may be compared to the OOP and IP LMCT bands, respectively. Gilbert *et al.* have previously demonstrated that the bandwidths and amplitudes of these bands, as well as the value of 10 Dq, may be determined by fitting the pre-edge to the sum of two Gaussians plus the tail of a third that accounts for the rising edge.<sup>58</sup>

To this end, we measured the oxygen K-edge absorption spectrum of a hematite thin film sample grown by ALD on a 200 nm thick  $\text{Si}_3\text{N}_4$  window in transmission mode in the ground state and 200 ps following excitation at 400 nm. Measurements were performed at beamline 6.0.2 at the Advanced Light Source (Lawrence Berkeley National Laboratory), and experimental details are provided in Section S8 of the ESI.<sup>†</sup> The data were analyzed as described for the variable temperature optical absorption experiment: the steady-state spectrum was fit, in this case to the sum of three Gaussians, and the XTA difference spectrum was then fit to the expression given by eqn (1). The results are collected in Table S3 (ESI<sup>†</sup>), and the steady-state and difference fits are shown in Fig. 6. The individual components of the difference fit are plotted in Fig. S6 (ESI<sup>†</sup>), clearly showing the pre-edge bands broaden and shift toward lower energies. Furthermore, the  $t_{2g}$  band broadens and shifts more than the  $e_g$  band, resulting in a  $170\text{ cm}^{-1}$  increase in 10 Dq. This quantitative agreement with the thermal optical absorption experiment is perhaps surprising, as the optical transitions involve different donor orbitals while the X-ray transitions originate from the oxygen 1s core. Nevertheless, our results agree with the molecular orbital energies of hematite clusters calculated by Debnath and Anderson, which show the iron 3d orbitals shift down in energy as the lattice expands while the oxygen 2s and 2p orbitals energies remain unshifted.<sup>60</sup> This observation is consistent with the more expanded and contracted radial wavefunctions of the valence and core orbitals, respectively. Overall, the trends observed in the oxygen pre-edge are in excellent agreement with those observed in the optical regime, supporting our assertion that lattice heating is

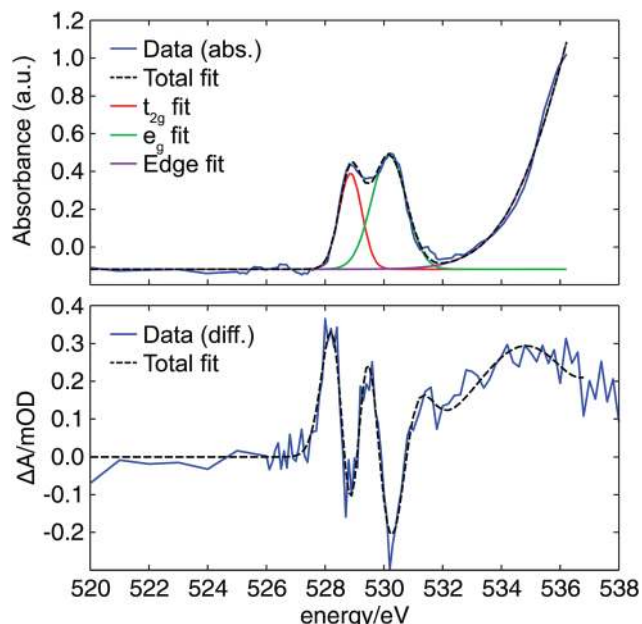


**Fig. 6** (top) The pre-edge of the oxygen K-edge absorption spectrum of a hematite thin film (blue). The spectrum was fit (dashed black) to the sum of three Gaussians representing the  $t_{2g}$  and  $e_g$  bands and the rising edge (red, green, and purple, respectively). (bottom) The pre-edge transient absorption spectrum (blue) obtained at delay of 200 ps following excitation at 400 nm, and the fit (dashed black) obtained using eqn (1) and the steady-state fit shown in the top panel. The fit parameters are collected in Table S3 (ESI $^\dagger$ ).

responsible for much of the transient signal detected upon optical excitation of hematite thin films and reinforcing our assignment of the optical absorption spectrum.

#### 4. Iron K-edge transient absorption

The iron K-edge XANES spectra of high spin octahedral iron oxides generally show an edge shift of approximately  $-1.5$  eV in going from ferric to ferrous oxides.<sup>61</sup> Accordingly, we sought to measure the XTA spectrum of hematite at the iron K-edge with the expectation that the contribution to the difference spectrum from the edge shift accompanying excitation of the LMCT band would be clearly distinguishable from the nuclear contributions arising from lattice heating. Measurements were performed at beamline 11-ID-D<sup>62–64</sup> at the Advanced Photon Source (APS) at Argonne National Laboratory, and experimental details are given in Section S9 of the ESI $^\dagger$ . The XTA difference spectrum at 100 ps following excitation at 351 nm is plotted alongside the XANES thermal difference spectrum (500 K minus 300 K) in Fig. 7, showing that while the majority of the features observed in the XTA spectrum are reproduced in the thermal spectrum, the relative amplitudes of the negative features at 7.129 and 7.133 keV disagree between the thermal and the XTA experiments.

To identify the origin of this difference, we evaluated several different possible models of a hot and/or electronically excited hematite lattice by calculating XANES spectra using the full multiple scattering code in the FEFF9 software package

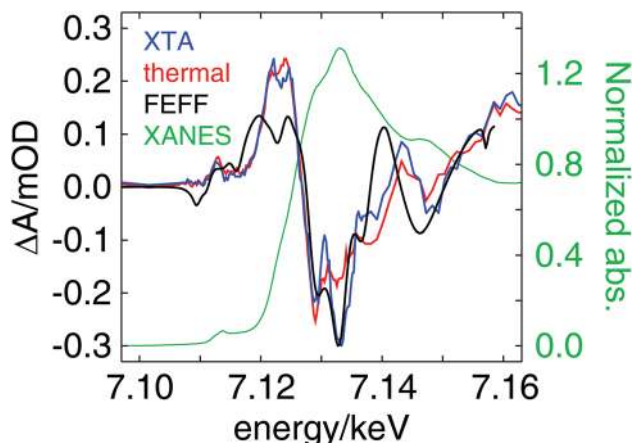


**Fig. 7** The iron K-edge thermal difference spectrum, obtained by taking the difference of the steady-state spectra measured at 500 K and 300 K (red), plotted alongside the XTA spectrum measured at a delay time of 100 ps with a pump wavelength of 351 nm (blue). The XANES spectrum is also shown (green) for comparison. The theoretical difference spectrum obtained from full multiple scattering calculations of hematite with and without an expanded lattice and increased thermal disorder is shown in black.

(see Section S10 of the ESI $^\dagger$  for details).<sup>65,66</sup> These models included: (1) an edge shift of  $-1.4$  eV to approximate the  $\text{Fe}^{2+}$  spectrum; (2) a configurationally averaged electron small polaron with and without a  $-1.4$  eV edge shift; (3) increased thermal disorder (Debye–Waller factors); (4) a thermally expanded lattice; and (5) a thermally expanded lattice with increased thermal disorder. A detailed description of these models is given in the ESI $^\dagger$  and a comparison of the calculated difference spectra is shown in Fig. S8 (ESI $^\dagger$ ). Generally, the difference spectra of the models that include an edge shift show poor agreement with the experimental spectrum and do not reproduce the strong negative feature at 7.133 keV. Thus, we conclude that the contributions of electron small polarons or other transient  $\text{Fe}^{2+}$  species to the difference spectrum is not significant.

On the other hand, the strictly thermal models gave difference spectra that show good qualitative agreement with the data. The spectrum calculated for the Debye–Waller model reproduces all of the peaks seen in the XANES spectrum including the two strong negative features, indicating that simply an increase in thermal disorder resulting from ultrafast lattice heating is responsible for much of the XTA signal. The calculated spectrum shows significantly weaker amplitude in the positive features at 7.122 and 7.125 keV compared to the XTA spectrum, while the experimental thermal difference spectrum agrees well in this region, suggesting that the appropriate picture includes both thermal disorder and lattice distortions. Indeed, the combined model that includes disorder and expansion shows improved agreement over the disorder-only model, and this calculation is plotted in Fig. 7 (black). We note that Sanson *et al.* observed largely anisotropic mean square relative displacements for only the short Fe–O bonds in molecular dynamics simulations, while our model is purely isotropic and homogeneous.<sup>67</sup>



Furthermore, because the thermal difference spectrum is a steady-state measurement, it includes contributions from both thermal disorder and an expanded lattice at equilibrium, which may not be representative of the hot lattice on the ultrafast timescale as expansion is occurring.<sup>14,68</sup> Nevertheless, these calculations demonstrate that the Fe K-edge XTA spectrum, like the oxygen K-edge XTA and visible OTA spectra, is dominated by lattice heating.

### 5. Optical transient absorption dynamics

While the transient spectra measured in the visible, soft X-ray, and hard X-ray regimes arise largely due to lattice heating, the broad, near-featureless positive signal measured in the red and NIR regions of the spectrum were not observed in the thermal difference spectrum (*vide supra*). This disparity could arise due to a distinction between steady-state and ultrafast heating, as observed for the iron K-edge XTA, or it could indicate that the NIR signal is purely due to the presence of new spin-allowed d-d transitions in the transient species. Accordingly, we investigated the dynamics of the visible and NIR OTA signals, which are shown in Fig. 8. The transients taken at probe wavelengths of 595 and 1050 nm with 415 nm excitation were fit to the sum of four exponential decays, as determined from singular value decomposition analysis, plus a constant offset and a Gaussian coherent artifact, all convolved with an instrument response function determined to be 190 fs from fits across all probe wavelengths. The transients could not be fit across all orders of

magnitude in time with fewer components, and our results agree well with those reported in the literature.<sup>3,5</sup>

The fits show remarkable agreement between the two probe wavelengths, indicating that the same dynamics are relevant for both the visible and NIR positive signals. This result is consistent with the work reported by Zhang and coworkers.<sup>2</sup> In the case of the visible TA spectrum, we also observe a strong, broad feature centered near 675 nm (labeled E) at very early time delays that largely decays within a few ps, leaving only the long tail of the main positive peak in this region at times beyond 100 ps. This behavior is shown in Fig. 9, in which each transient spectrum is normalized to its maximum. The shift of peak D to bluer wavelengths on the few ps timescale occurs as a result of the decay of the broad feature at 675 nm, which likely contributes to the positive signal in the 550–600 nm region. Meanwhile, the structure in region C between 450 and 550 nm, where the broad feature likely does not contribute, remains fixed in position. We do observe a partial decay of the negative signal in region C on the same timescale, however, which is consistent with the loss of GSB and/or SE signal following recombination. Within 250 ps, the spectrum is essentially indistinguishable in shape from the spectrum at 3 ns or the thermal difference spectrum. The shape and location of the short-lived absorption band at 675 nm is consistent with that observed by Durrant and coworkers at very long (> 1 ms) delay times only under *in situ* conditions with a positive external potential,<sup>44,45</sup> meaning an applied bias is necessary to extend the lifetime of the species responsible for this ESA feature beyond the ultrafast regime.

Within the context of these observations and the thermal and photoinduced XANES difference spectra, we are able to form a

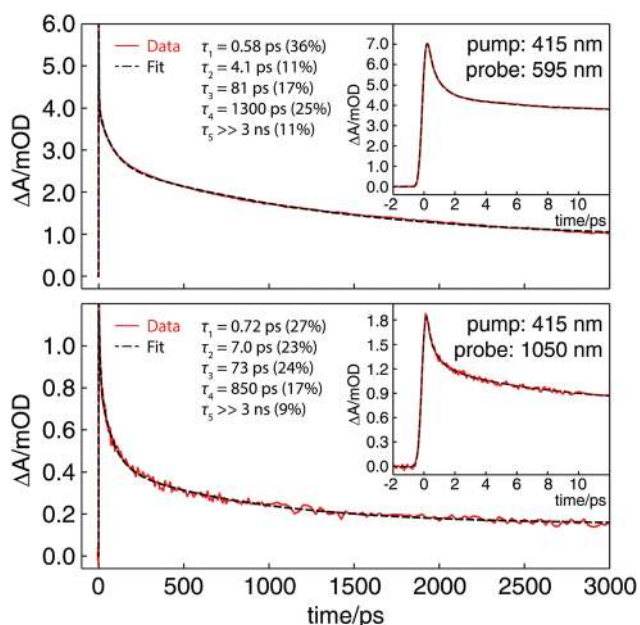


**Fig. 8** Kinetic traces (red) taken from the optical (top) and NIR (bottom) transient absorption spectra of a hematite thin film following excitation at 415 nm. The regions that were averaged to give the traces are shown in Fig. 2, with average probe wavelengths given above. The traces were each fit (dashed black) to the sum of four exponential decays ( $\tau_1$ – $\tau_4$ ) plus a Gaussian coherent artifact and a constant offset ( $\tau_5$ ), all convolved with a Gaussian IRF. The time constants and percentages of the fit components are also shown. Insets show the kinetic traces and fits at early delay times.

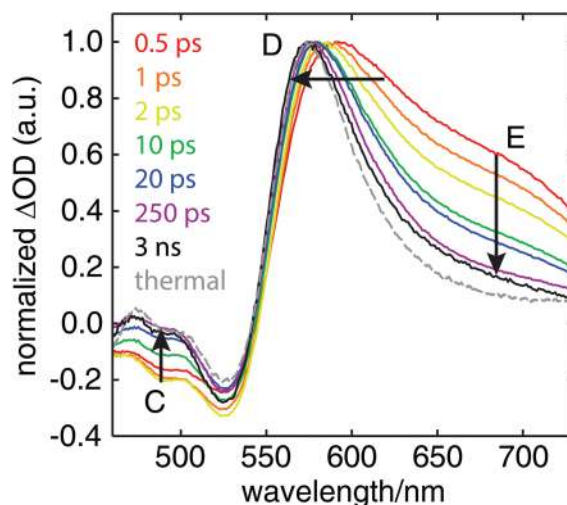


**Fig. 9** A series of OTA spectra of a hematite thin film following excitation at 415 nm normalized to their respective maxima to highlight the evolution of the spectral shape. Features referenced in the main text are labeled C–E. A broad ESA band at ~675 nm (E) appears at early times but decays within 100 ps, and subsequent spectra do not show significant further changes. This feature is assigned to free carrier absorption, and the 80 ps time constant obtained from the fits in Fig. 8 is assigned to carrier recombination, which also causes the decay of the GSB signal in region C.



picture of the dynamics in hematite following laser excitation. The sub-ps and few-ps time constants likely encompass a number of processes, including carrier–carrier scattering, carrier–phonon scattering, impact ionization, and polaron formation, which ultimately yield a hot lattice with thermalized free carriers within 10 ps.<sup>3,51,69–72</sup> Next, carrier recombination occurs on a timescale of  $\sim 75$  ps, in agreement with previous reports<sup>2,3,50</sup> and the 59 ps relaxation time observed in aqueous  $[\text{Fe}(\text{H}_2\text{O})_6]^{3+}$  (see Fig. S9, ESI†). The broad ESA feature at 675 nm (E), then, likely corresponds to absorption by hot and thermalized conduction band electrons as well as hole filling in the valence band, in keeping with the assignment of Durrant and coworkers.<sup>6</sup> The  $\sim 1$  ns component may correspond to non-geminate recombination and carrier trapping occurring during carrier diffusion and/or the propagation of lattice expansion<sup>13,14,73</sup> as the Fe–O bonds approach their high-temperature equilibrium bond lengths. Because the iron K-edge XTA spectrum measured at 100 ps does not perfectly match the thermal difference spectrum or the calculated difference spectra for models including only lattice expansion or thermal disorder, we believe that the latter process – dynamic lattice expansion – is primarily responsible for the  $\sim 1$  ns lifetime observed in the OTA spectra. The final time component, which aggregates any components longer than the 3 ns temporal window of this experiment, is included in the fits as a constant offset. This term may also include contributions from residual free carriers, but the striking agreement between the OTA spectrum at 3 ns and the thermal difference spectrum indicates that this term arises predominantly due to the slow cooling of the lattice back to room temperature.<sup>12</sup>

To investigate this long time component in greater detail, we performed an additional series of OTA measurements in the ns and  $\mu\text{s}$  regimes (see Section S11 of the ESI† for details). The transient spectra at several delay times following excitation at 425 nm are shown in Fig. 10 (left), with the kinetic trace measured at 595 nm shown in Fig. 10 (right). The spectrum

shifts to shorter wavelengths as it decays, capturing the retreat of the LMCT bands back to their room temperature frequencies as the lattice cools. The fit to the kinetic trace, which gives an IRF of 0.27 ns, includes a 1.5 ns time constant, in agreement with the ultrafast OTA data, as well as slower components with lifetimes of 10 and 82 ns, all in excellent agreement with those measured by Huang *et al.*<sup>5</sup> Finally, we observe a 1.5  $\mu\text{s}$  component and a small offset even at 30  $\mu\text{s}$ ; the small transient remaining at 25  $\mu\text{s}$ , which has a maximum of  $\sim 0.3$  mOD, is shown in Fig. 10 (left). Again, all lifetimes beyond 1.5 ns likely correspond almost entirely to lattice cooling and not carrier recombination as previously assigned.<sup>3,5,46</sup> Even at early times ( $< 1$  ns), the spectrum does not show the broad feature observed in the ultrafast OTA at delays less than 100 ps, but the tail of the positive peak extends into the NIR. Because there is a gap between 750 and 950 nm in the white light visible and NIR continuum probes used in the ultrafast OTA, we also measured the ns OTA signal from 700 to 1000 nm to verify that the signal observed in this region (F) on the ns timescale is simply the extension of the tail of the primary positive feature (D) and does not show any additional structure. These spectra are plotted in Fig. S11 (ESI†).

The dynamics observed in the picosecond and nanosecond OTA spectra are illustrated in Scheme 1, which shows five snapshots of the band structure of hematite at different times following excitation. In the first panel, a valence band electron absorbs a photon (blue arrow), yielding a hot carrier in the conduction band. The second panel depicts carrier thermalization at 1 ps, during which the hot electron relaxes within the conduction band by transferring energy to the lattice through phonon emission (red arrow). The band gap shrinks as a result of the absorption of thermal energy by the lattice, as shown by the dashed arrows between the second and third panels. At 10 ps, free carrier absorption (orange arrow) gives rise to the ESA peak at 675 nm. Recombination occurs on a similar timescale and is complete within 100 ps. While there are no

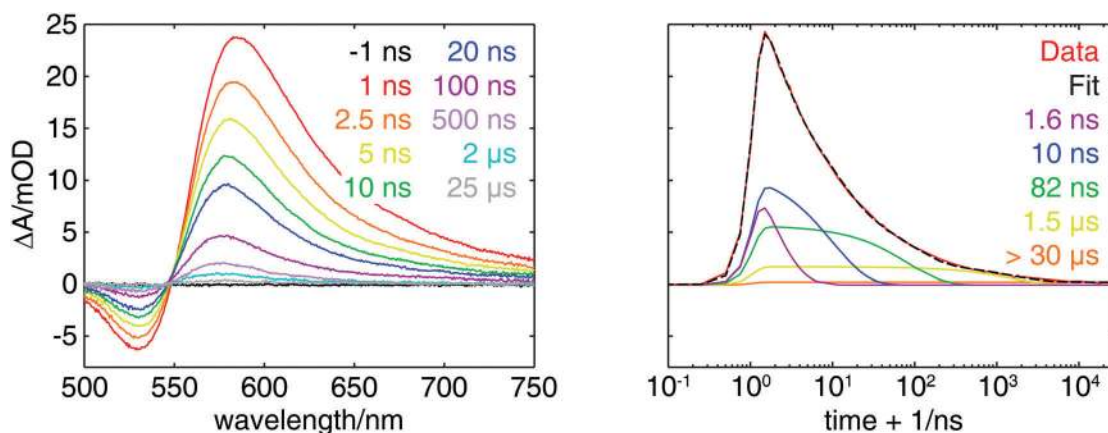
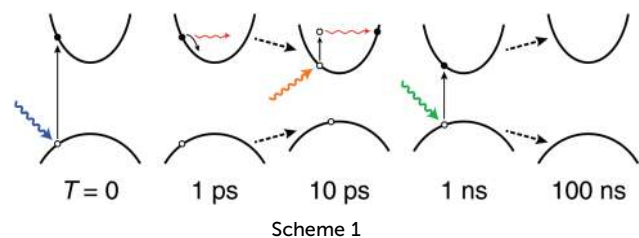


Fig. 10 (left) The long-time OTA spectra of a hematite thin film following excitation at 425 nm. The maximum of the ESA shifts toward shorter wavelengths as the signal decays, corresponding to the shift of the LMCT bands back to room temperature frequencies as the lattice cools. A small transient is still observed as late as 25  $\mu\text{s}$ . (right) The kinetic trace (red) taken by averaging over the same probe wavelength used to obtain the ultrafast trace shown in Fig. 8, plotted on a logarithmic scale. The trace was fit (dashed black) to the sum of four exponential decays plus a weak constant offset. The individual fit components are also plotted and the corresponding time constants provided.



Scheme 1

free carriers left at 1 ns, the band gap remains narrower, giving rise to a bathochromic shift of the ground state absorption (green arrow) as shown in the fourth panel. We stress that this transient signal corresponds to ground state absorption by the hot lattice, and thus we do not refer to the signal as ESA as is the convention for positive signals in transient absorption measurements. Finally, lattice cooling on the timescale of 100 ns returns the band edges to their room temperature positions, as shown by the dashed arrows connecting the fourth and fifth panels.

## 6. Insensitivity of transient signals to excitation and morphology

The optical, NIR, soft X-ray, and hard X-ray transient absorption measurements were also performed with several different excitation wavelengths spanning the optical absorption spectrum of hematite in an attempt to distinguish signals arising from LMCT and d-d transitions. These results are shown in Fig. S12–S14 (ESI<sup>†</sup>). For each regime, the spectra are nearly identical for all excitation wavelengths, further demonstrating that the transients predominantly arise due to lattice heating as a result of carrier-phonon scattering that occurs as hot carriers thermalize in the conduction band, a process that occurs for both LMCT transitions and transitions between the  $t_{2g}$  and  $e_g$  bands.<sup>72</sup> Although we have assigned the short-lived ESA peak at 675 nm (E) to free carrier absorption, this feature is too broad and overlaps too closely with the tail of the positive peak (D) that arises from the shift of the LMCT bands to permit a reliable comparison of its position or line shape for different excitations. We note that even at the extremes of the absorption spectrum of hematite – at 277 nm, which should exclusively excite LMCT transitions, and at 830 nm, which should exclusively excite d-d transitions – we find remarkable agreement across all spectral regimes probed in both the shape of the transient spectra and the time constants obtained to fits of the kinetic traces taken at several probe wavelengths.

Finally, we consider the contribution of surface defects to the transient spectra presented in this work. Taking the linear Fe–Fe distance to be approximately 4 Å on average, surface irons should only account for approximately 4% of the total sample probed for the 20 nm films used in this work. However, because the surface sites could disproportionately account for the transient signal, we investigated this possibility by performing OTA measurements on a mull sample prepared from powdered bulk hematite and a 20 nm hematite thin film coated with a 2 nm layer of  $Al_2O_3$  to passivate surface defects. The transient spectra obtained for these samples are shown in Fig. S16

and S17 (ESI<sup>†</sup>), and they clearly exhibit the same features and kinetics as observed for the bare hematite thin films. Furthermore, the OTA spectra of thicker hematite thin films prepared by molecular beam epitaxy reported in the literature<sup>3</sup> also show excellent agreement with our data, and we therefore conclude that the transient spectra do not exhibit a significant dependence on morphology in going from the bulk scale to the 20 nm scale. This result is indeed expected, given that the OTA data can be largely assigned to lattice heating.

## Discussion

### 1. Transient absorption methods for solid state samples: challenges and opportunities

Transient absorption measurements of hematite, and similarly any other extended solid for which the lattice is comprised of the absorber being probed in the time-resolved measurement, present a formidable challenge in the isolation of signals corresponding to excited state electronic structure from those corresponding to thermally induced structural distortions. The transient spectra of a dilute absorber in a bath that is in resonance with neither the pump nor the probe – for example, a chromophore in a protein or a small molecule in a solvent – correspond exclusively to the sub-ensemble of absorbers in the excited state. While these spectra are modulated by nuclear wave packet motion on the excited state potential energy surface and the exchange of energy with the bath,<sup>74</sup> to a first approximation these dynamics are not coupled to the sub-ensemble that remains in the ground state, and thus the ground state absorbers do not contribute to the transient signal.

In the case of hematite and many other metal oxide semiconductors, however, the ground state sub-ensemble is the bath with which the excited state species exchange energy, and the transient signal will therefore include contributions from distorted metal sites in the electronic ground state, regardless of the morphology of the sample. This problem is further compounded by the fact that this energy exchange occurs locally and therefore inhomogeneously throughout the material on the ultra-fast timescale,<sup>14</sup> potentially giving rise to an intractably large number of spectroscopically active species to consider when modeling the data. The difficulty of probing the electronic dynamics of a metal center in the solid phase is readily demonstrated by comparing the shape and kinetics of the transient spectra of  $[Fe(H_2O)_6]^{3+}$  in aqueous solution and drop cast on fused quartz (see Fig. S9, S10 and S15, ESI<sup>†</sup>). The aqueous complex fully relaxes within 200 ps with kinetics that are fit well after the first picosecond by only a single 59 ps time constant. Meanwhile, the drop cast film exhibits a broad transient extending into the NIR with multi-exponential kinetics that persist well beyond 3 ns comparable to that observed for hematite thin films. Nevertheless, a 61 ps time constant is among those obtained in a fit of the kinetics of the drop cast  $[Fe(H_2O)_6]^{3+}$  film, demonstrating that electronic relaxation can still be observed even in the presence of a large background that arises from lattice heating and supporting our

assignment of the  $\sim 75$  ps time constant measured for hematite to carrier recombination.

On the other hand, charge carrier injection, diffusion, and localization processes have been successfully investigated through transient absorption studies of dye-sensitized semiconductor nanomaterials in the optical,<sup>50,75</sup> X-ray,<sup>48,49,63,75,76</sup> and terahertz<sup>77</sup> regimes. These systems are more amenable to techniques utilizing ultrafast optical pulses because the structural dynamics of the absorbing species are decoupled from the solid material. In the case of OTA or XTA in which the X-ray probe is tuned to the absorption edge of the metal in the dye, the probe selectively monitors the electronic state of the dye to give an indirect measure of charge injection and back-transfer rates, thereby circumventing the inherent difficulties of modeling the solid entirely. In the case of terahertz transient absorption or XTA in which the X-ray probe is tuned to the absorption edge of the metal in the semiconductor, the species being pumped (the dyes adsorbed to the semiconductor surface) and the species being probed (free carriers in the conduction band of the semiconductor) are distinct, assuming that the semiconductor does not absorb any of the excitation pulse. Consequently, these techniques can give a direct measure of charge carrier dynamics while minimizing photoinduced lattice heating. Even for these systems, however, carrier injection is accompanied by carrier-phonon scattering, so thermal effects cannot be entirely discounted. Furthermore, the XANES spectrum of a metal is very sensitive to local environment, and thus modeling the spectrum of a polaronic distortion requires both an accurate picture of the distortion and a configurational average over all absorbers within the extent of the propagation of the distortion.

While it is difficult to conclusively identify signals from electronic excited states in XTA measurements of solid-state metal oxide materials using temporally broad X-ray pulses from storage rings, sub-ps X-ray pulses from slicing beamlines,<sup>78</sup> X-ray free electron lasers,<sup>79</sup> and tabletop high harmonic generation schemes<sup>80</sup> offer the opportunity to probe these systems during the carrier thermalization process. Using a fs tabletop XUV probe pulse, Vura-Weis *et al.* observed a shift of  $\sim 2.5$  eV in the  $M_{2,3}$ -edge of a hematite thin film immediately following excitation at 400 nm, a result consistent with the photoinduced reduction of  $Fe^{3+}$  to  $Fe^{2+}$  expected for an LMCT transition.<sup>51</sup> The M-edge difference spectrum was shown to evolve with a 240 fs time constant, however, to a final shape consistent with neither an LMCT nor a d-d excited state that persists for the 3.5 ps window of the experiment. This result is consistent with the sub-ps time constant observed in the OTA kinetics presented in this work, which we have assigned to carrier thermalization and polaron formation processes and the attendant local lattice heating. Because the iron K-edge XTA experiments presented here were conducted by necessity at the 100 ps timescale, we do not observe a similar 1.4–2.5 eV edge shift, as the signal is overwhelmed by thermal effects after only a few tens of ps. Consequently, it is not possible to quantify relative contributions from LMCT and d-d transitions for different excitation wavelengths from these data for the purpose of

mapping the positions of absorption bands across the optical spectrum of hematite, but sub-ps XTA experiments may provide a means of achieving this goal.

## 2. Assignment of steady state and transient absorption features of hematite

Although the multi-wavelength transient absorption measurements presented here do not reliably distinguish between LMCT and d-d transitions in hematite, the combined steady-state and time-resolved spectroscopic data and complementary theoretical calculations support an assignment of the optical spectrum in which both the OOP and IP LMCT bands extend across the near UV and much of the visible, consistent with recent experimental<sup>51</sup> and theoretical<sup>39</sup> treatments. From both the optical and oxygen K-edge transient spectra, we observe band gap shrinkage consistent with a model in which these LMCT bands shift to lower energies as the lattice expands. In the case of hematite, lattice expansion – whether from photo-induced lattice heating or not – results in anisotropic Fe–O bond elongation,<sup>56,67,81</sup> thereby distorting the iron sites even further from octahedral symmetry and increasing the degree of mixing among the frontier orbitals. Ultimately this expansion causes the LMCT bands to broaden and shift to lower energies, as demonstrated to a first approximation through DFT calculations on isolated  $[Fe(H_2O)_6]^{3+}$  complexes. Thermal band gap shrinkage is well known in semiconductors, although the relative contributions to this phenomenon from lattice expansion, thermal disorder, and polaronic self-energy vary depending on the material.<sup>15–17,70</sup> Our efforts to model the iron K-edge XTA spectra demonstrate that at least a combination of lattice expansion and thermal disorder contribute significantly to laser-induced band gap shrinkage in hematite thin films as early as 100 ps following excitation (see Fig. S8, ESI†). Because the transient signal beyond 100 ps is essentially identical to the thermal difference spectrum, we do not expect that band gap renormalization following conduction band edge filling plays a significant role.<sup>82–84</sup>

Our assignment of the optical absorption spectrum of hematite fully agrees with that presented by Chernyshova *et al.*<sup>43</sup> In their work, the authors assign each of the d-d bands to specific transitions from the  $d^5$  Tanabe–Sugano diagram. We do not undertake such a detailed assignment here and instead refer the reader to their assignments and those collected from the literature in their meta-study. More importantly, we emphasize the magnitude and breadth of the LMCT bands and the position of the OOP band near 400 nm in this model. The lower energy LMCT band, and not a collection of d-d bands, is responsible for the strong, protruding feature in the absorption spectrum in this region. On the other hand, we find that the sharp rise in absorption near 550 nm does in fact correspond to a group of d-d bands. This distinction is significant because it allows us to separately estimate the direct and the indirect band gaps of hematite.<sup>29,58,85</sup> While this general assignment has been proposed as early as 1963,<sup>35</sup> other assignments continue to find support in the literature.<sup>41,86</sup> Our work here provides a new body of evidence that strongly supports a model

of the absorption spectrum in which two LMCT bands span from the NUV to almost 600 nm, and this understanding allows us to assess different hypotheses regarding the photoelectrochemical activity of the material.

### 3. Wavelength dependence of photocatalysis in hematite

The mechanism of photoelectrochemical water oxidation by hematite remains an open question.<sup>4,24,87–89</sup> However, the increase in both the APCE and IPCE spectra at bluer wavelengths suggests that the transient species generated by LMCT transitions are significantly more photochemically active than those generated by d–d transitions.<sup>29</sup> One possible explanation for this is that the initial LMCT state, in which the electron is in an iron 3d orbital and the hole is in an oxygen 2p orbital, facilitates subsequent charge separation and diffusion through the lattice. In comparison, the electron and hole are co-localized within the iron 3d orbitals following excitation of a d–d transition, resulting in greater loss of efficiency to charge recombination. Our model cannot address this mechanistic hypothesis, and wavelength-dependent *in situ* studies will be necessary to quantify recombination losses for different absorption bands. However, we may calculate a theoretical IPCE curve for our model of the optical spectrum with the ansatz that only LMCT transitions yield photocurrent to determine if this hypothesis fits the data.

Using the fit of the absorption spectrum shown in Fig. 1, we take the sum of the LMCT absorption bands, convert from optical density to fraction of photons absorbed, and multiply by the fraction of incident photons that are not reflected by the sample, as determined from the reflectance spectrum (see Section S12 of the ESI† for details). The resulting theoretical IPCE spectrum is shown in Fig. 11 (black curve) with the light

harvesting efficiency spectrum (LHE) provided as a reference (green curve). The calculated IPCE spectrum shows excellent agreement with the experimental IPCE curve measured by Huang *et al.* (not depicted), with both showing a maximum at 370 nm and a local minimum at 315 nm at 77% the amplitude of the maximum.<sup>5</sup> From our model, we may attribute this drop in efficiency at 315 nm to absorption by the d–d bands at 318 and 290 nm. We note this drop was also observed by Hamann and coworkers for hematite thin films grown by both ALD and electrodeposition.<sup>34</sup> We also note that the band from 500–550 nm in the LHE spectrum does not appear in the calculated IPCE spectrum, as this absorption is attributed to photochemically inactive d–d transitions. While both the calculated and experimental spectra show the IPCE drop off dramatically by 540 nm, a weak tail persists in the calculated spectrum out to nearly 700 nm. Because the reflectance-corrected absorption spectrum is poorly resolved beyond 600 nm, our model does not include the lower energy d–d bands that have been reported elsewhere.<sup>37,38</sup> Consequently, the tails of the broad LMCT bands, albeit very weak in this region, surpass the resolved d–d bands in amplitude at 587 nm, while realistically the lower energy d–d bands likely account for the majority of the absorption from 600 to 700 nm. Additionally, some of the LMCT oscillator strength in the red part of the spectrum may correspond to transitions to intraband trap states,<sup>6</sup> which are not expected to yield photocurrent.

### 4. Prospects for improving photocatalytic performance

The agreement between the calculated and experimental IPCE spectra suggest that the d–d transitions are indeed not photochemically active, while both LMCT transitions contribute to the photocurrent with approximately equal quantum efficiencies. Our calculated spectrum corresponds to quantum efficiencies of 100% for the LMCT transitions, but we may obtain an estimate of the actual LMCT quantum yield by comparing the absolute scale of the calculated spectrum to experimental data. Taking the IPCE values at 370 nm of the calculated (42%) and experimental<sup>5</sup> (24%) spectra, we find the LMCT-to-current efficiency to be 57%, meaning that more than half of all LMCT transitions yield photocurrent under the conditions of the experimental measurement (1 M NaOH and a bias of 1.43 V vs. RHE). Fig. 11 also shows the IPCE curve calculated for the 500 K absorption spectrum (red curve), which exhibits a significant red shift ( $\sim 20$  nm) due to shrinkage of the band gap. Although conducting bulk photoelectrochemical oxidation of water at 500 K is obviously impractical, it may be possible to prepare thin films of hematite with an expanded lattice similar to that measured at high temperature that are stable under ambient conditions by inducing strain through grain boundaries, doping,<sup>30,42,90–92</sup> or isomorphically templated ALD. Emery *et al.* have successfully prepared thin films of epitaxially stabilized  $\beta$ -Fe<sub>2</sub>O<sub>3</sub>, which is normally thermodynamically unstable under the conditions of deposition.<sup>93</sup> Such work demonstrates the feasibility of employing a similar technique to shift the LMCT absorption bands of hematite further into the visible part of the spectrum and thereby improve overall photoelectrochemical performance.

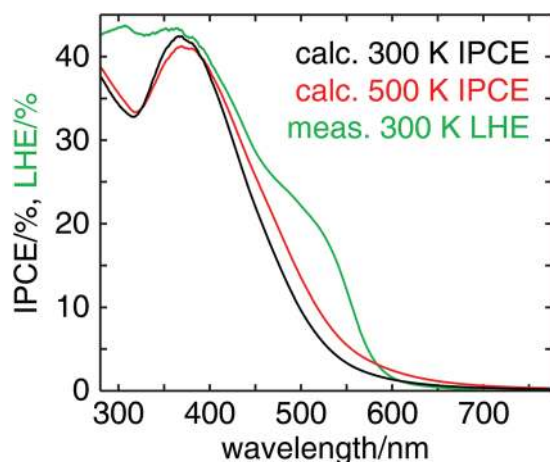


**Fig. 11** The theoretical IPCE curves calculated for an LMCT-only model of photocatalytic oxygen evolution at 100% quantum efficiency for a 20 nm hematite thin film at 300 K (black) and 500 K (red) based on the fit to the steady-state absorption spectrum shown in Fig. 1 and the reflectivity spectrum shown in Fig. S1 (ESI†). This model assumes all LMCT excitations yield photocurrent while all d–d excitations do not. The black spectrum shows excellent agreement with the experimental IPCE spectrum reported by Huang *et al.* The light harvesting efficiency spectrum (green) is shown as a reference.



*In situ* electrochemical experimental conditions provide both a bias to drive charge separation and a sink for photocarriers, while the *ex situ* conditions of the work presented here necessitate that all photocarriers ultimately recombine. We do not observe a significant difference in the relaxation rates for the hematite thin film and aqueous  $[\text{Fe}(\text{H}_2\text{O})_6]^{3+}$ , and thus we conclude that an external potential is necessary to achieve substantial charge separation across the lattice and accumulate a population of free carriers with lifetimes long enough to participate in interfacial chemistry. A comparison of the broad ESA feature at 675 nm (E) that we observe only at early delay times ( $<100$  ps) and a similar feature observed by Durrant and coworkers at both short ( $<1$  ns)<sup>47</sup> and long ( $>1$  ms)<sup>44,45</sup> delay times only under an applied external bias supports our conclusion that nearly all photocarriers in hematite recombine within a few hundred ps under *ex situ* illumination and the transient signals observed beyond this time are largely, if not entirely, due to the expansion and cooling of the lattice. We note that the *in situ* OTA spectra measured on the ms timescale are markedly different in shape than the *ex situ* spectra; because the lattice returns to room temperature within tens of  $\mu\text{s}$  following laser excitation, only photocarriers contribute to the TA signal at later times. With this in mind, we look toward future wavelength-dependent time-resolved work conducted *in situ* in both the optical and X-ray regimes to highlight differences in the ultrafast carrier relaxation and separation dynamics following LMCT and d-d excitations under an external potential. Braun *et al.* have successfully measured the steady-state X-ray absorption spectrum of hematite at the oxygen K-edge *in situ*, demonstrating the feasibility of performing similar measurements in a time-resolved fashion.<sup>94</sup>

## Conclusions

Investigating mechanisms of heterogeneous photocatalysis using time-resolved spectroscopies is inherently challenging. The short laser pulses needed to generate a coherent excited state population large enough to detect with subsequent probe pulses unavoidably introduce a substantial amount of thermal energy into the system that leads to a complex cascade of processes reflected in the kinetics of transient absorption signals. Thermal disorder, dynamic lattice expansion, and ultimately lattice cooling may all drastically affect the optical and X-ray absorption spectra of the material in the same manner that temperature-dependent vibrational and spin occupancy and structural distortions manifest in the absorption spectra of small molecules, thereby partially or fully obscuring the contributions from transient electronic excited states that are the targets of these studies. In fact, we have demonstrated here that the transient absorption signals in hematite thin films spanning from the NIR to the optical, soft X-ray, and even hard X-ray regimes are dominated by these thermal contributions within the first 100 ps following excitation. However, we have taken advantage of these large spectral changes due to ultrafast temperature jumps in order to gain more fundamental insight into the correlation between the nuclear structure of the lattice and the electronic structure of the material and how these can be manipulated to improve photoelectrochemical performance.

By comparing transient absorption spectra to variable temperature steady-state absorption spectra, we have been able to assign many of the consistent features to particular perturbations in the electronic structure of the hematite films arising from lattice heating. We have also been able to detect a broad excited state absorption feature unique to the optical transient absorption that decays within 100 ps and have assigned this feature to free carrier absorption in agreement with previous spectroelectrochemical measurements. The collective results support a model of the optical absorption spectrum of hematite with two broad LMCT bands spanning from the NUV nearly across the visible with several weaker d-d bands distributed between 300 nm and the NIR. Thermally induced structural distortions involve anisotropic Fe-O bond elongation, resulting in a marked red-shift in the absorption spectrum. Stabilizing similar distortions at ambient temperature could therefore lead to an increase in photon-to-current efficiency across the solar spectrum.

Deep understanding of photoelectrochemical water oxidation in hematite will benefit from optical and X-ray transient absorption measurements conducted *in situ* with time delays spanning from the sub-ps to the ms regime. But while these experiments will naturally amplify the electronic signals of interest by minimizing photocarrier recombination, care must still be taken to distinguish these signals from thermal contributions.

## Acknowledgements

This work was supported by the U.S. Department of Energy, Office of Science, Office of Basic Energy Sciences, through Argonne National Laboratory (ANL) under Contract No. DE-AC02-06CH11357. D. H. acknowledges support from the Joseph J. Katz Fellowship from ANL. Use of the Advanced Photon Source (APS) at ANL is supported by the U.S. Department of Energy, Office of Science, Office of Basic Energy Sciences under Contract No. DE-AC02-06CH11357. A. A. C., R. W. S., and experiments at the Advanced Light Source (ALS) at Lawrence Berkeley National Laboratory were supported by the U.S. Department of Energy, Office of Science, Office of Basic Energy Sciences under Contract No. DE-AC02-05CH11231. Work by J. D. E. and A. B. M. F., including project conception, ALD thin film growth, and discussion was supported by Argonne-Northwestern Solar Energy Research (ANSER) Center, an Energy Frontier Research Center funded by the U.S. Department of Energy, Office of Science, Office of Basic Energy Sciences, under Award Number DE-SC0001059. We gratefully acknowledge the computing resources provided on Blues and Fusion, a high-performance computing cluster operated by the Laboratory Computing Resource Center at ANL.

## Notes and references

- 1 N. S. Lewis and D. G. Nocera, *Proc. Natl. Acad. Sci. U. S. A.*, 2006, **103**, 15729–15735.
- 2 N. J. Cherepy, D. B. Liston, J. A. Lovejoy, H. Deng and J. Z. Zhang, *J. Phys. Chem. B*, 1998, **102**, 770–776.

- 3 A. G. Joly, J. R. Williams, S. A. Chambers, G. Xiong, W. P. Hess and D. M. Laman, *J. Appl. Phys.*, 2006, **99**, 053521.
- 4 A. J. Cowan, C. J. Barnett, S. R. Pendlebury, M. Barroso, K. Sivula, M. Grätzel, J. R. Durrant and D. R. Klug, *J. Am. Chem. Soc.*, 2011, **133**, 10134–10140.
- 5 Z. Huang, Y. Lin, X. Xiang, W. Rodriguez-Cordoba, K. J. McDonald, K. S. Hagen, K.-S. Choi, B. S. Brunschwig, D. G. Musaev, C. L. Hill, D. Wang and T. Lian, *Energy Environ. Sci.*, 2012, **5**, 8923–8926.
- 6 M. Barroso, S. R. Pendlebury, A. J. Cowan and J. R. Durrant, *Chem. Sci.*, 2013, **4**, 2724–2734.
- 7 M. Zhang, M. de Respinis and H. Frei, *Nat. Chem.*, 2014, **6**, 362–367.
- 8 J. C. Polanyi and A. H. Zewail, *Acc. Chem. Res.*, 1995, **28**, 119–132.
- 9 L. X. Chen, in *X-Ray Absorption and X-Ray Emission Spectroscopy*, ed. J. A. V. Bokhoven and C. Lamberti, John Wiley & Sons, Ltd, Hoboken, NJ, 2016, pp. 213–249.
- 10 T. Glaser, B. Hedman, K. O. Hodgson and E. I. Solomon, *Acc. Chem. Res.*, 2000, **33**, 859–868.
- 11 M. Ross, B. E. V. Kuiken, M. L. Strader, A. Cordones-Hahn, H. Cho, R. W. Schoenlein, T. K. Kim and M. Khalil, in *Ultrafast Phenomena XIX*, ed. K. Yamanouchi, S. Cundiff, R. de Vivie-Riedle, M. Kuwata-Gonokami and L. DiMauro, Springer International Publishing, Cham, Switzerland, 2015, pp. 403–406.
- 12 S. K. Sundaram and E. Mazur, *Nat. Mater.*, 2002, **1**, 217–224.
- 13 C. Rose-Petrucci, R. Jimenez, T. Guo, A. Cavalleri, C. W. Siders, F. Rksi, J. A. Squier, B. C. Walker, K. R. Wilson and C. P. J. Barty, *Nature*, 1999, **398**, 310–312.
- 14 S. Stoupin, A. M. March, H. Wen, D. A. Walko, Y. Li, E. M. Dufresne, S. A. Stepanov, K.-J. Kim, Y. V. Shvyd'ko, V. D. Blank and S. A. Terentyev, *Phys. Rev. B: Condens. Matter Mater. Phys.*, 2012, **86**, 054301.
- 15 P. Lautenschlager, P. B. Allen and M. Cardona, *Phys. Rev. B: Condens. Matter Mater. Phys.*, 1985, **31**, 2163–2171.
- 16 S. Abdollahi Pour, B. Movaghar and M. Razeghi, *Phys. Rev. B: Condens. Matter Mater. Phys.*, 2011, **83**, 115331.
- 17 Y.-J. Li, S. Ye, C.-H. Wang, X.-M. Wang and Q.-Y. Zhang, *J. Mater. Chem. C*, 2014, **2**, 10395–10402.
- 18 O. Durmeyer, J. P. Kappler, E. Beaurepaire, J. M. Heintz and M. Drillon, *J. Phys.: Condens. Matter*, 1990, **2**, 6127.
- 19 S. Nozawa, T. Iwazumi and H. Osawa, *Phys. Rev. B: Condens. Matter Mater. Phys.*, 2005, **72**, 121101.
- 20 O. Durmeyer, E. Beaurepaire, J.-P. Kappler, C. Brouder and F. Baudelet, *J. Phys.: Condens. Matter*, 2010, **22**, 125504.
- 21 D. Manuel, D. Cabaret, C. Brouder, P. Sainctavit, A. Bordage and N. Trcera, *Phys. Rev. B: Condens. Matter Mater. Phys.*, 2012, **85**, 224108.
- 22 A. B. F. Martinson, M. J. DeVries, J. A. Libera, S. T. Christensen, J. T. Hupp, M. J. Pellin and J. W. Elam, *J. Phys. Chem. C*, 2011, **115**, 4333–4339.
- 23 M. J. Katz, S. C. Riha, N. C. Jeong, A. B. F. Martinson, O. K. Farha and J. T. Hupp, *Coord. Chem. Rev.*, 2012, **256**, 2521–2529.
- 24 K. M. H. Young, B. M. Klahr, O. Zandi and T. W. Hamann, *Catal. Sci. Technol.*, 2013, **3**, 1660.
- 25 J. H. Kennedy and K. W. Frese, *J. Electrochem. Soc.*, 1978, **125**, 709–714.
- 26 M. P. Dare-Edwards, J. B. Goodenough, A. Hamnett and P. R. Trevellick, *J. Chem. Soc., Faraday Trans. 1*, 1983, **79**, 2027–2041.
- 27 M. G. Walter, E. L. Warren, J. R. McKone, S. W. Boettcher, Q. Mi, E. A. Santori and N. S. Lewis, *Chem. Rev.*, 2010, **110**, 6446–6473.
- 28 O. Zandi and T. W. Hamann, *Phys. Chem. Chem. Phys.*, 2015, **17**, 22485–22503.
- 29 A. Kay, I. Cesar and M. Grätzel, *J. Am. Chem. Soc.*, 2006, **128**, 15714–15721.
- 30 I. Cesar, K. Sivula, A. Kay, R. Zboril and M. Grätzel, *J. Phys. Chem. C*, 2009, **113**, 772–782.
- 31 Y. Lin, S. Zhou, S. W. Sheehan and D. Wang, *J. Am. Chem. Soc.*, 2011, **133**, 2398–2401.
- 32 C. X. Kronawitter, L. Vayssieres, S. Shen, L. Guo, D. A. Wheeler, J. Z. Zhang, B. R. Antoun and S. S. Mao, *Energy Environ. Sci.*, 2011, **4**, 3889–3899.
- 33 S. C. Riha, M. J. DeVries Vermeer, M. J. Pellin, J. T. Hupp and A. B. F. Martinson, *ACS Appl. Mater. Interfaces*, 2013, **5**, 360–367.
- 34 O. Zandi, A. R. Schon, H. Hajibabaei and T. W. Hamann, *Chem. Mater.*, 2016, **28**, 765–771.
- 35 R. F. G. Gardner, F. Sweett and D. W. Tanner, *J. Phys. Chem. Solids*, 1963, **24**, 1183–1196.
- 36 J. A. Tossell and D. J. Vaughan, *Am. Mineral.*, 1974, **59**, 319–334.
- 37 L. A. Marusak, R. Messier and W. B. White, *J. Phys. Chem. Solids*, 1980, **41**, 981–984.
- 38 D. M. Sherman and T. D. Waite, *Am. Mineral.*, 1985, **70**, 1262–1269.
- 39 P. Liao and E. A. Carter, *J. Phys. Chem. C*, 2011, **115**, 20795–20805.
- 40 N. Pailhé, A. Wattiaux, M. Gaudon and A. Demourgues, *J. Solid State Chem.*, 2008, **181**, 1040–1047.
- 41 N. Pailhé, A. Wattiaux, M. Gaudon and A. Demourgues, *J. Solid State Chem.*, 2008, **181**, 2697–2704.
- 42 M. Gaudon, N. Pailhé, J. Majimel, A. Wattiaux, J. Abel and A. Demourgues, *J. Solid State Chem.*, 2010, **183**, 2101–2109.
- 43 I. V. Chernyshova, S. Ponnurangam and P. Somasundaran, *Phys. Chem. Chem. Phys.*, 2010, **12**, 14045–14056.
- 44 S. R. Pendlebury, A. J. Cowan, M. Barroso, K. Sivula, J. Ye, M. Grätzel, D. R. Klug, J. Tang and J. R. Durrant, *Energy Environ. Sci.*, 2012, **5**, 6304–6312.
- 45 M. Barroso, C. A. Mesa, S. R. Pendlebury, A. J. Cowan, T. Hisatomi, K. Sivula, M. Grätzel, D. R. Klug and J. R. Durrant, *Proc. Natl. Acad. Sci. U. S. A.*, 2012, **109**, 15640–15645.
- 46 S. Sorenson, E. Driscoll, S. Haghighat and J. M. Dawlaty, *J. Phys. Chem. C*, 2014, **118**, 23621–23626.
- 47 S. R. Pendlebury, X. Wang, F. Le Formal, M. Cornuz, A. Kafizas, S. D. Tilley, M. Grätzel and J. R. Durrant, *J. Am. Chem. Soc.*, 2014, **136**, 9854–9857.

- 48 J. E. Katz, B. Gilbert, X. Zhang, K. Attenkofer, R. W. Falcone and G. A. Waychunas, *J. Phys. Chem. Lett.*, 2010, **1**, 1372–1376.
- 49 J. E. Katz, X. Zhang, K. Attenkofer, K. W. Chapman, C. Frandsen, P. Zarzycki, K. M. Rosso, R. W. Falcone, G. A. Waychunas and B. Gilbert, *Science*, 2012, **337**, 1200–1203.
- 50 B. Gilbert, J. E. Katz, N. Huse, X. Zhang, C. Frandsen, R. W. Falcone and G. A. Waychunas, *Phys. Chem. Chem. Phys.*, 2013, **15**, 17303–17313.
- 51 J. Vura-Weis, C.-M. Jiang, C. Liu, H. Gao, J. M. Lucas, F. M. F. de Groot, P. Yang, A. P. Alivisatos and S. R. Leone, *J. Phys. Chem. Lett.*, 2013, **4**, 3667–3671.
- 52 J. Ferguson and P. E. Fielding, *Chem. Phys. Lett.*, 1971, **10**, 262–265.
- 53 J. B. Baxter, C. Richter and C. A. Schmuttenmaer, *Annu. Rev. Phys. Chem.*, 2014, **65**, 423–447.
- 54 A. Cotton and M. D. Meyers, *J. Am. Chem. Soc.*, 1960, **82**, 5023–5026.
- 55 L. W. Finger and R. M. Hazen, *J. Appl. Phys.*, 1980, **51**, 5362–5367.
- 56 A. F. Gualtieri and P. Venturelli, *Am. Mineral.*, 1999, **84**, 895–904.
- 57 Z. Y. Wu, S. Gota, F. Jollet, M. Pollak, M. Gautier-Soyer and C. R. Natoli, *Phys. Rev. B: Condens. Matter Mater. Phys.*, 1997, **55**, 2570–2577.
- 58 B. Gilbert, C. Frandsen, E. R. Maxey and D. M. Sherman, *Phys. Rev. B: Condens. Matter Mater. Phys.*, 2009, **79**, 035108.
- 59 C. X. Kronawitter, I. Zegkinoglou, S. Shen, J. Guo, F. J. Himpsel, S. S. Mao and L. Vayssieres, *Phys. Chem. Chem. Phys.*, 2013, **15**, 13483–13488.
- 60 N. C. Debnath and A. B. Anderson, *J. Electrochem. Soc.*, 1982, **129**, 2169–2174.
- 61 M. Wilke, F. Farges, P.-E. Petit, G. E. Brown and F. Martin, *Am. Mineral.*, 2001, **86**, 714–730.
- 62 G. Jennings, W. J. H. Jäger and L. X. Chen, *Rev. Sci. Instrum.*, 2002, **73**, 362–368.
- 63 X. Zhang, G. Smolentsev, J. Guo, K. Attenkofer, C. Kurtz, G. Jennings, J. V. Lockard, A. B. Stickrath and L. X. Chen, *J. Phys. Chem. Lett.*, 2011, **2**, 628–632.
- 64 L. X. Chen and X. Zhang, *J. Phys. Chem. Lett.*, 2013, **4**, 4000–4013.
- 65 J. J. Rehr, J. J. Kas, M. P. Prange, A. P. Sorini, Y. Takimoto and F. Vila, *C. R. Phys.*, 2009, **10**, 548–559.
- 66 J. J. Rehr, J. J. Kas, F. D. Vila, M. P. Prange and K. Jorissen, *Phys. Chem. Chem. Phys.*, 2010, **12**, 5503–5513.
- 67 A. Sanson, O. Mathon and S. Pascarelli, *J. Chem. Phys.*, 2014, **140**, 224504.
- 68 K. Sokolowski-Tinten, J. Bialkowski, A. Cavalleri, D. von der Linde, A. Oparin, J. Meyer-ter-Vehn and S. I. Anisimov, *Phys. Rev. Lett.*, 1998, **81**, 224–227.
- 69 M. Breusing, C. Ropers and T. Elsaesser, *Phys. Rev. Lett.*, 2009, **102**, 086809.
- 70 C. V. Shank, R. L. Fork, R. F. Leheny and J. Shah, *Phys. Rev. Lett.*, 1979, **42**, 112–115.
- 71 H. M. Fan, G. J. You, Y. Li, Z. Zheng, H. R. Tan, Z. X. Shen, S. H. Tang and Y. P. Feng, *J. Phys. Chem. C*, 2009, **113**, 9928–9935.
- 72 T.-Y. Chen, C.-H. Hsia, H. S. Son and D. H. Son, *J. Am. Chem. Soc.*, 2007, **129**, 10829–10836.
- 73 E. Collet, N. Moisan, C. Baldé, R. Bertoni, E. Trzop, C. Lahlé, M. Lorenc, M. Servol, H. Cailleau, A. Tissot, M.-L. Boillot, T. Graber, R. Henning, P. Coppens and M. B.-L. Cointe, *Phys. Chem. Chem. Phys.*, 2012, **14**, 6192–6199.
- 74 B. S. Prall, D. Y. Parkinson, N. Ishikawa and G. R. Fleming, *J. Phys. Chem. A*, 2005, **109**, 10870–10879.
- 75 J. Huang, O. Buyukcakir, M. W. Mara, A. Coskun, N. M. Dimitrijevic, G. Barin, O. Kokhan, A. B. Stickrath, R. Ruppert, D. M. Tiede, J. F. Stoddart, J.-P. Sauvage and L. X. Chen, *Angew. Chem., Int. Ed.*, 2012, **51**, 12711–12715.
- 76 M. H. Rittmann-Frank, C. J. Milne, J. Rittmann, M. Reinhard, T. J. Penfold and M. Chergui, *Angew. Chem., Int. Ed.*, 2014, **53**, 5858–5862.
- 77 L. A. Martini, G. F. Moore, R. L. Milot, L. Z. Cai, S. W. Sheehan, C. A. Schmuttenmaer, G. W. Brudvig and R. H. Crabtree, *J. Phys. Chem. C*, 2013, **117**, 14526–14533.
- 78 R. W. Schoenlein, S. Chattopadhyay, H. H. W. Chong, T. E. Glover, P. A. Heimann, C. V. Shank, A. A. Zholents and M. S. Zolotarev, *Science*, 2000, **287**, 2237–2240.
- 79 H. T. Lemke, C. Bressler, L. X. Chen, D. M. Fritz, K. J. Gaffney, A. Galler, W. Gawelda, K. Haldrup, R. W. Hartsock, H. Ihee, J. Kim, K. H. Kim, J. H. Lee, M. M. Nielsen, A. B. Stickrath, W. K. Zhang, D. L. Zhu and M. Cammarata, *J. Phys. Chem. A*, 2013, **117**, 735–740.
- 80 L. Nugent-Glandorf, M. Scheer, D. A. Samuels, V. Bierbaum and S. R. Leone, *Rev. Sci. Instrum.*, 2002, **73**, 1875–1886.
- 81 A. Sanson, A. Zaltron, N. Argiolas, C. Sada, M. Bazzan, W. G. Schmidt and S. Sanna, *Phys. Rev. B: Condens. Matter Mater. Phys.*, 2015, **91**, 094109.
- 82 H. Kalt and M. Rinker, *Phys. Rev. B: Condens. Matter Mater. Phys.*, 1992, **45**, 1139–1154.
- 83 A. Walsh, J. L. F. Da Silva and S.-H. Wei, *Phys. Rev. B: Condens. Matter Mater. Phys.*, 2008, **78**, 075211.
- 84 A. Chernikov, C. Ruppert, H. M. Hill, A. F. Rigosi and T. F. Heinz, *Nat. Photonics*, 2015, **9**, 466–470.
- 85 Y. Ma, P. D. Johnson, N. Wassdahl, J. Guo, P. Skytt, J. Nordgren, S. D. Kevan, J.-E. Rubensson, T. Böske and W. Eberhardt, *Phys. Rev. B: Condens. Matter Mater. Phys.*, 1993, **48**, 2109–2111.
- 86 R. V. Pisarev, A. S. Moskvina, A. M. Kalashnikova and T. Rasing, *Phys. Rev. B: Condens. Matter Mater. Phys.*, 2009, **79**, 235128.
- 87 P. Liao, J. A. Keith and E. A. Carter, *J. Am. Chem. Soc.*, 2012, **134**, 13296–13309.
- 88 F. Le Formal, E. Pastor, S. D. Tilley, C. A. Mesa, S. R. Pendlebury, M. Grätzel and J. R. Durrant, *J. Am. Chem. Soc.*, 2015, **137**, 6629–6637.
- 89 Y. Zhang, H. Zhang, H. Ji, W. Ma, C. Chen and J. Zhao, *J. Am. Chem. Soc.*, 2016, **138**, 2705–2711.
- 90 S. S. Shinde, R. A. Bansode, C. H. Bhosale and K. Y. Rajpure, *J. Semicond.*, 2011, **32**, 013001.

- 91 L. Carroll, P. Friedli, S. Neuenschwander, H. Sigg, S. Cecchi, F. Isa, D. Chrastina, G. Isella, Y. Fedoryshyn and J. Faist, *Phys. Rev. Lett.*, 2012, **109**, 057402.
- 92 N. Mirbagheri, D. Wang, C. Peng, J. Wang, Q. Huang, C. Fan and E. E. Ferapontova, *ACS Catal.*, 2014, **4**, 2006–2015.
- 93 J. D. Emery, C. M. Schlepütz, P. Guo, S. C. Riha, R. P. H. Chang and A. B. F. Martinson, *ACS Appl. Mater. Interfaces*, 2014, **6**, 21894–21900.
- 94 A. Braun, K. Sivula, D. K. Bora, J. Zhu, L. Zhang, M. Grätzel, J. Guo and E. C. Constable, *J. Phys. Chem. C*, 2012, **116**, 16870–16875.